Inorganic Chemistry

ARTICLE

pubs.acs.org/IC

Multiple Structures and Dynamics of $[CpRu(CO)_2]_2$ and $[CpFe(CO)_2]_2$ in Solution Revealed with Two-Dimensional Infrared Spectroscopy

Jessica M. Anna, John T. King, and Kevin J. Kubarych*

Department of Chemistry, University of Michigan, 930 North University Avenue, Ann Arbor, Michigan 48197, United States

S *Supporting Information*

ABSTRACT: Two-dimensional infrared (2DIR) spectroscopy is applied to both $(Cp)_2Fe_2(CO)_4$ and its ruthenium analog $(Cp)_2Ru_2(CO)_4$ in order to study the vibrational dynamics of these two systems. Combining the results of 2DIR spectroscopy and DFT calculations, the different structural forms of both the iron and the ruthenium complexes were characterized, furthering the previous assignment of the linear IR spectrum by determining the transition frequencies associated with the different isomeric forms. Monitoring the time-dependent amplitudes of the cross peaks enabled the observation of equilibrium energy transfer dynamics between different vibrational modes of the *cis*-B $(Cp)_2Fe_2(CO)_4$ and the *gauche*-NB $(Cp)_2Ru_2(CO)_4$ complexes. Treating the energy transfer as an equilibrium process, we extracted the rate constants associated with both the uphill and the downhill transfer of vibrational energy, finding that the difference in the rate constants of the two metal complexes maps to the difference in the energy gap between the two modes involved.

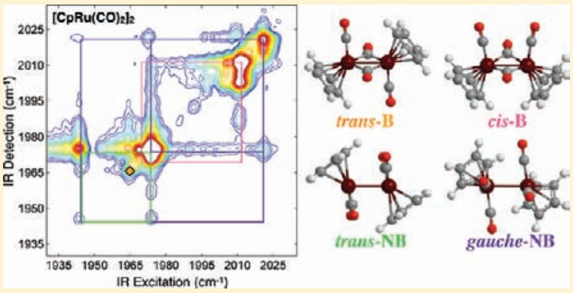

INTRODUCTION

Determination of the structure, reactivity, dynamics, and photoproducts of transition metal complexes in solution is challenging due to their often flexible nature, connecting multiple reactant species with several photochemical products.[1] Resolving structure and dynamics in mixtures of reactants, intermediates, and products is a challenge that has recently been met by two-dimensional infrared (2DIR) spectroscopy to examine electronic ground[2] and excited states[3] as well as photoproducts,[1e,f,2c] intermediates,[1c] and rebinding reactions.[2c] Here, we apply 2DIR spectroscopy to two different group 8 metal carbonyl compounds, cyclopentadienyliron dicarbonyl dimer and its ruthenium analog. These complexes are structurally similar but mainly differ in the distance between the two metal atoms. Applying 2DIR spectroscopy to these complexes we fully resolve the congested IR spectrum while obtaining otherwise inaccessible information on the transfer of vibrational energy between vibrational modes. We recently found that in extended metal carbonyl complexes the transfer of vibrational excitation among the carbonyl stretching bands is a sensitive probe of solvent−solute interactions that perturb the energetic symmetry of the local carbonyl units.[4] We also used 2DIR spectroscopy along with DFT results to obtain detailed information on the structure and energetics of the different species.

Binuclear $Cp_2Fe_2(CO)_4$ and the ruthenium analog $Cp_2Ru_2(CO)_4$ have been studied for over 50 years.[5] One motivation for ongoing investigations of these complexes arises from the dynamical and structural complexity of fluxional interconversion between multiple isomeric forms. Earlier IR,[6] X-ray crystallography,[7] and NMR[6g,8] studies identified and characterized these different structures, finding that $Cp_2Fe_2(CO)_4$ exists primarily as two isomers in equilibrium at room temperature while $Cp_2Ru_2(CO)_4$ exists as four isomers (Figure 1).[6e−g] More recently $Cp_2Fe_2(CO)_4$ and $Cp_2Ru_2(CO)_4$ have been studied because of the rich photochemistry that accompanies the presence of multiple isomers in equilibrium.[9]

To further the study of these systems we applied two-dimensional infrared (2DIR) spectroscopy to both $Cp_2Fe_2(CO)_4$ and $Cp_2Ru_2(CO)_4$. 2DIR spectroscopy spreads the information contained in a linear Fourier transform IR (FTIR) spectrum over two frequency axes. Cross peaks in the 2DIR spectrum provide both high frequency and time resolution, allowing a direct probe of energy transfer between two different chemical species or among different modes of the same species, along with information regarding the assignment of the peaks in the linear IR spectrum. 2DIR spectroscopy has been used to study a number of fundamental phenomena including chemical exchange, intramolecular vibrational energy redistribution, hydrogen bonding, protein conformation changes, and spectral diffusion.[2a,b,10a,10b,10d−10f,10h] In this manuscript we apply 2DIR spectroscopy to both $Cp_2Fe_2(CO)_4$ and $Cp_2Ru_2(CO)_4$.

Using 2DIR spectroscopy, we observed intramolecular vibrational energy redistribution (IVR) between different modes of the *cis*-B isomer of $Cp_2Fe_2(CO)_4$ and the *gauche*-NB isomer of $Cp_2Ru_2(CO)_4$. Treating IVR as an equilibrium process we obtain the IVR rate constants associated with both the uphill and the ownhill transfer of energy. We find that the rate of IVR varies

Received: March 7, 2011
Published: August 29, 2011

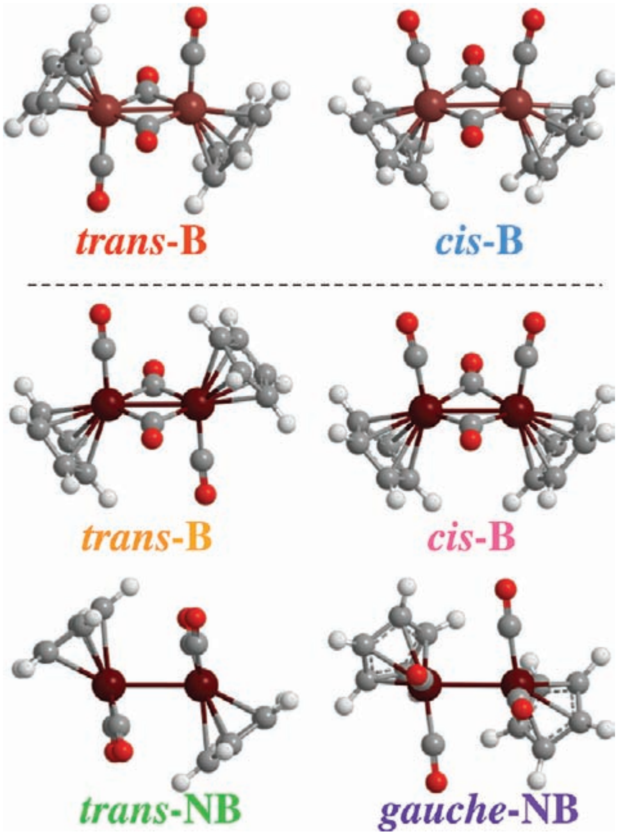

Figure 1. Equilibrium structures for both $Cp_2Fe_2(CO)_4$ (top) and $Cp_2Ru_2(CO)_4$ (bottom).

between the two metal species and that the difference in the rate maps to the difference in energy between the two states exchanging vibrational excitation. In addition to exploring energy transfer dynamics, we also used 2DIR spectroscopy along with DFT calculations to obtain a detailed understanding of the energetics of the different species. By analyzing the detailed cross-peak locations we obtain the transition frequencies of the different isomeric forms for both the iron and the ruthenium complex. Using density functional theory (DFT) calculations we obtain the relative energies of the different isomers of $Cp_2Fe_2(CO)_4$ and $Cp_2Ru_2(CO)_4$ along with the structures and energies of the transition states connecting the stable isomers. Combining the DFT and experimental results we are able to obtain a detailed picture of the differences between the two metal complexes.

EXPERIMENTAL AND THEORETICAL METHODS

I. Experimental Methods. 2DIR spectroscopy spreads the information contained in a linear IR spectrum over two frequency axes, ω_{excite} and ω_{detect}, resulting in a frequency−frequency correlation map.[11] The detected signal results from the interaction of three 100 fs excitation pulses with the sample. The first excitation pulse creates a coherence that serves to effectively label each molecule. The arrival of the second pulse creates either a population or an excited state coherence ending the t_1 time period and marking the beginning of the t_2 time period, the waiting time. The system evolves during the waiting time, which ends upon arrival of the third excitation pulse. The third excitation pulse marks the beginning of the t_3 time period by creating another coherence, effectively recording the final state of each molecule labeled during t_1. A Fourier transform along t_1 and t_3 results in the ω_{excite} and ω_{detect} axes.

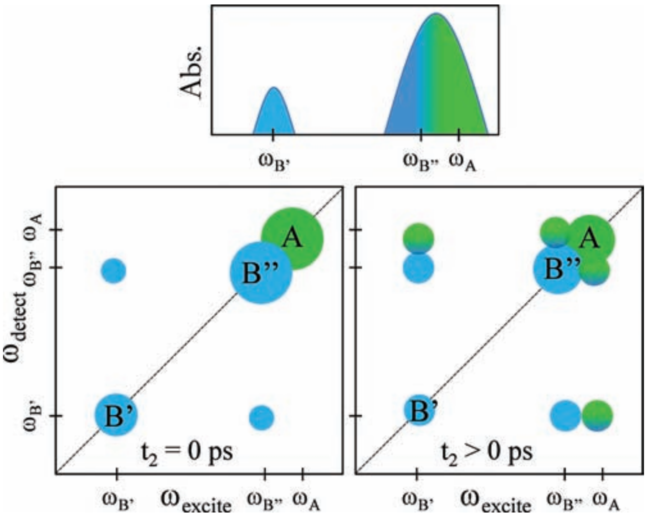

Figure 2. Schematic 2DIR spectra at different waiting times along with a corresponding schematic of the linear FTIR spectrum indicating overlapping bands.

Cartoon 2DIR spectra with a corresponding linear spectrum are shown in Figure 2. The spectra consist of two species, A and B, where A has one absorption feature at frequency ω_a and B has two absorptions at $\omega_{b'}$ and $\omega_{b''}$. The linear spectrum consists of two peaks, and there is no indication that the higher frequency peak has two contributions from different species. In the 2D spectrum, peaks lying along the diagonal correspond to those in the linear spectrum. At $t_2 = 0$ ps, in the absence of intermolecular energy transfer, which is typically the case for dilute solutions, features in the 2DIR spectrum such as cross peaks are only due to pairs of transitions that belong to the same molecule (or molecular species), that is, in a dilute mixture of multiple species). That is impossible to observe cross peaks between different species unless there is chemical exchange. The cross peaks present at $t_2 = 0$ ps, which we denote "inherent cross peaks", arise because the two transitions have a common ground state and lie within the bandwidth of the excitation and detection pulses. It is important to note, in the case of very fast exchange, where the barrier is ~1 kcal/mol or less, exchange may occur during the coherence period, leading to cross peaks at $t_2 = 0$ ps between different chemical species.[12] However, when the barrier to exchange is a few kcal/mol, the system does not undergo exchange during the coherence period and lacks exchange cross peaks at $t_2 = 0$ ps.[2a,13] The iron and ruthenium metal−carbonyl systems studied fall within this regime; therefore, we do not consider the fast exchange scenario in this manuscript, and cross peaks at $t_2 = 0$ ps are assigned to inherent cross peaks, indicating that the corresponding diagonal peaks belong to the same species.

In the cartoon 2D spectrum at $t_2 = 0$ ps there are inherent cross peaks arising from the two transitions of species B. For species B, the transition frequency of the higher frequency mode can be determined from the ω_{detect} frequency of the cross peak. In this way the 2DIR spectrum can be used to effectively gain spectral resolution in the sense that the transition frequencies can be determined from the cross peaks, whereas they could not be determined unambiguously from the linear spectrum. Previous studies have demonstrated the use of 2DIR spectroscopy to aid in the assignment of linear spectra,[14] though in the present case the multiple species are not in principle separable since they are different equilibrium structures of the same molecules.

The amplitudes of the peaks will change as the time between excitation and detection (t_2) is increased. All the peaks in the spectrum will decay due to molecular reorientation and population relaxation, while some peaks will grow or appear due to intramolecular vibrational energy transfer and/or chemical exchange. It is specifically this "waiting

Table 1. 2DIR Experimentally Determined Frequencies and Scaled DFT-Calculated Frequencies for Both $Cp_2Fe_2(CO)_4$ and $Cp_2Ru_2(CO)_4$

	exp. frequencies (cm^{-1})	DFT frequencies (cm^{-1})
$Cp_2Fe_2(CO)_4$		
trans-B	1962.0 ± 0.1	1961.8
cis-B	1965.0 ± 0.6	1967.5
	2006.9 ± 0.1	2003.0
$Cp_2Ru_2(CO)_4$		
trans-B	1965.8 ± 0.1	1966.6
cis-B	1970	1971.5
	2011.2 ± 0.1	2007.8
gauche-NB	1942.4 ± 1.3	1948.9, 1949.3
	1972.4 ± 0.1	1970.2
	2020.8 ± 0.5	2015.7
trans-NB	1941.9 ± 0.5	1946.5
	1973.7 ± 0.1	1969.3

time" dependence that gives 2DIR spectroscopy its powerful ability to track chemical dynamics in solution.

The 2DIR spectra were collected using our method of chirped-pulse upconversion 2DIR spectroscopy that has been described in detail previously.[15] There are two phase matching conditions that are relevant for 2DIR spectroscopy which are referred to as the rephasing ($-k_1 + k_2 + k_3$) and nonrephasing ($+k_1 - k_2 + k_3$) spectra (a detailed explanation of rephasing and nonrephasing spectra is given in the Supporting Information). Since we are interested in extracting the rate of IVR from the inherent cross peaks we have chosen to use the nonrephasing spectra, eliminating the need to fit the waiting time-dependent oscillations present in absorptive and rephasing spectra. Waiting time-dependent nonrephasing spectra were recorded in varying t_2 steps. Details on waiting time step sizes and sample preparation are given in the Supporting Information.

II. Theoretical Methods. Density functional theory (DFT) calculations were performed on both $Cp_2Fe_2(CO)_4$ and $Cp_2Ru_2(CO)_4$ using Gaussian03.[16] All calculations were performed using the B3LYP functional. Basis set details are given in the Supporting Information. Previous studies have suggested the pathway for isomerization from *trans*-B to *cis*-B proceeds through nonbridging intermediates, *trans*-NB and *gauche*-NB.[6g] DFT calculations were performed on these isomers for both $Cp_2Fe_2(CO)_4$ and $Cp_2Ru_2(CO)_4$ and the transition states connecting the stable states specified by the suggested pathway. The transition states connecting the different isomers were determined using the synchronous transit-guided quasi Newton methods.[17] For each transition state a single imaginary frequency was obtained, and the transition states were confirmed by observing that the single imaginary frequency connected the two corresponding stable isomers. Frequency calculations were also performed. Table 1 displays the experimentally determined frequencies with the corresponding DFT-calculated frequencies scaled by 0.9636 for $Cp_2Fe_2(CO)_4$ and 0.9652 for $Cp_2Ru_2(CO)_4$. The theoretically determined frequencies only differ from the experimentally determined frequencies by ~7 cm^{-1}. The scaled DFT-calculated frequencies are also shown as dashed lines in Figure 3.

RESULTS AND DISCUSSION

I. Structure and Energetics. *A. $Cp_2Fe_2(CO)_4$.* The linear FTIR spectrum of $Cp_2Fe_2(CO)_4$ in the terminal carbonyl stretching region is shown in Figure 3a. Previous studies[6e] have assigned peak 1 at 1962 cm^{-1} to the *trans*-B isomer with a small contribution from the *cis*-B isomer. Peak 2 at 2007 cm^{-1} was assigned to the *cis*-B isomer. It has also been suggested that there is a small contribution, a negligible amount, of the *trans*-NB form present. The presence of the *trans*-NB form leads to absorption features in the linear IR spectrum at 1938, 1973, and 2015 cm^{-1}.[18] We do not see absorption features at these frequencies in our linear FTIR spectrum, indicating that the nonbridging form is not significantly populated at room temperature in *n*-hexane. The modes associated with these peaks are described in the Supporting Information.

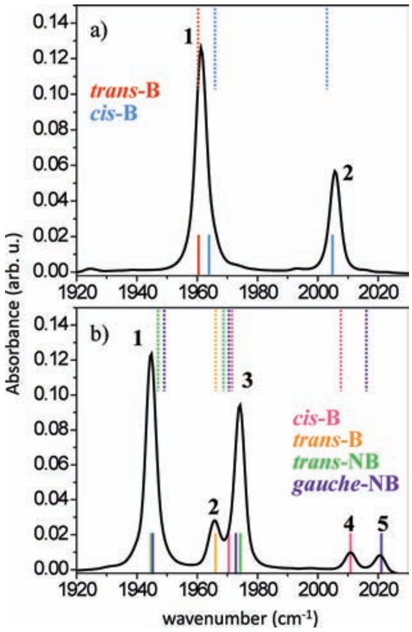

Figure 3. Linear FTIR spectra of $Cp_2Fe_2(CO)_4$ (a) and $Cp_2Ru_2(CO)_4$ (b) in *n*-hexane. Scaled DFT-calculated frequencies are indicated with dashed lines, and 2DIR experimentally determined frequencies are indicated with solid lines. The lines are color coded so that for the iron complex the blue lines correspond to the *cis*-B isomer and the red to the *trans*-B isomer. For the ruthenium complex, the pink lines correspond to the *cis*-B isomer, the orange to the *trans*-B isomer, the green to the *trans*-NB isomer, and the purple to the *gauche*-NB isomer.

The absolute value of the 2DIR nonrephasing spectra of $Cp_2Fe_2(CO)_4$ in hexane at t_2 = 200 fs and 10 ps are shown in Figure 4. The peaks lying along the diagonal, peaks 1 and 2, correspond to the two peaks in the linear FTIR spectrum. Peaks 1′ and 2′, which are shifted to slightly lower frequencies along ω_{detect}, are due to excited state absorptions and are red shifted due to the vibrational anharmonicity. Peaks 3 and 4 are present at t_2 = 200 fs, and as t_2 increases we see the appearance of peaks 4′ and 5. Figure 4 also displays an energy level diagram depicting information regarding the transition frequencies that can be obtained from the 2DIR spectrum for both the first and the second excited state manifolds. Table 2 gives the excitation and detection frequencies associated with the peaks. These values were obtained by fitting the peaks in slices taken from the 2D spectra to Lorentzian line shapes.

The 2DIR spectra of $Cp_2Fe_2(CO)_4$ confirm the assignment of the linear IR spectra. Cross peaks 4 and 5 are inherent cross peaks, arising because there are two transitions from the *cis*-B isomer lying within the ~200 cm^{-1} bandwidth of the incoming 100 fs pulses. Cross peak 5 is not present at t_2 = 200 fs due to the tuning of the incoming pulses. As t_2 increases, the amplitude of

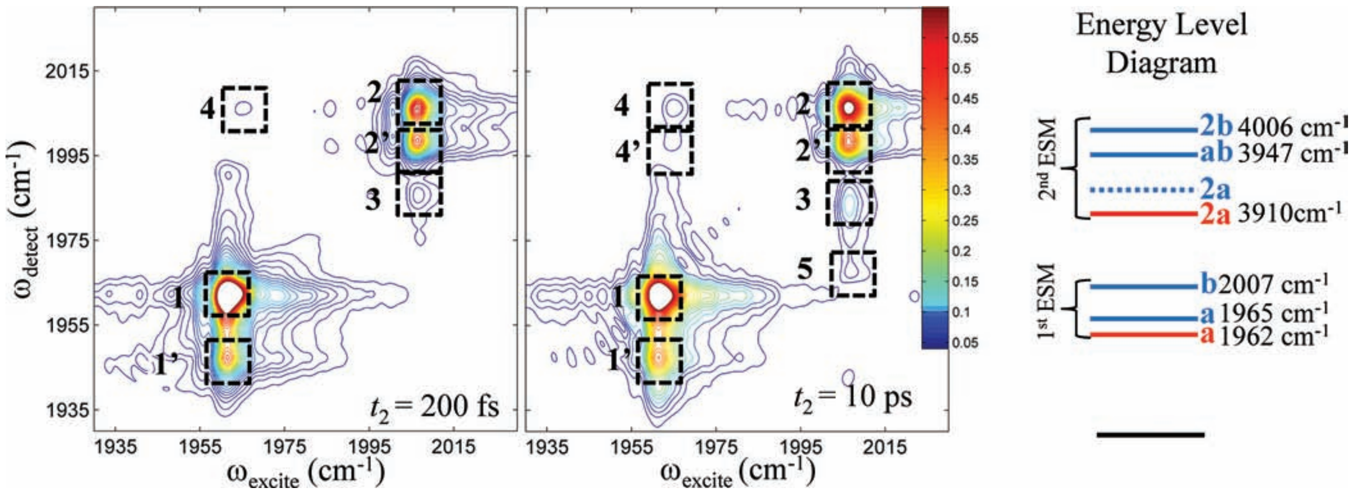

Figure 4. Absolute-value nonrephasing spectra of $Cp_2Fe_2(CO)_4$ in *n*-hexane at t_2 = 200 fs and 10 ps. Spectra are normalized to the maximum peak at the given t_2 value, and 30 contours are plotted for each spectrum.

Table 2. Excitation and Detection Frequencies Obtained by Fitting the Peaks in Slices Taken from the 2D Spectra to Lorentzian Line Shapes

peak	ω_{excite}	ω_{detect}
1	1962.0 ± 0.1	1962.0 ± 0.0
1′	1962.0 ± 0.1	1948.1 ± 0.1
2	2006.9 ± 0.1	2006.5 ± 0.0
2′	2006.8 ± 0.1	1998.4 ± 0.1
3	2007.0 ± 0.1	1981.6 ± 0.1
4	1965.0 ± 0.6	2006.6 ± 0.1
4′	1964.5 ± 0.6	1998.4 ± 0.1
5	2007.3 ± 0.5	1968.3 ± 0.4

cross peak 5 increases due to intramolecular vibrational energy redistribution between the two modes of the *cis*-B isomer. As shown with the cartoon spectra, we can obtain the transition frequency of the lower frequency mode of the *cis*-B isomer from the corresponding cross peak (cross peak 4). Taking a slice along ω_{excite} at ω_{detect} = 2007 cm^{-1} of the 2D spectrum we fit cross peak 4 to a Lorentzian obtaining a transition frequency of 1965.0 ± 0.6 cm^{-1} for the lower frequency mode of the *cis*-B isomer. We also determined the transition frequencies between the first and the second excited state manifolds from peaks 1′, 2′, 4′, and 3. Peaks 1′ and 2′ are due to excited state absorptions. The difference between the shifted peaks and the corresponding diagonal peaks is a measure of the vibrational anharmonicity. Peak 1′ is shifted by 14 cm^{-1} along ω_{detect} compared to peak 1, and peak 2′ is shifted by 8 cm^{-1} with respect to peak 2. From the anharmonicites, the frequencies of the second excited states 2a (red line) and 2b (blue line) (Figure 4) are found to be 3910 cm^{-1} for 2a and 4006 cm^{-1} for 2b. Peak 3 is due to transitions from the first excited state manifold of the *cis*-B isomer (a and b, Figure 4 blue lines) to the corresponding combination band (ab, Figure 4 blue line). Peak 4′, which has the same ω_{detect} frequency as peak 2′, arises because intramolecular vibrational energy transfer has occurred between the two modes of the *cis*-B isomer; population has been transferred from the lower frequency mode (a Figure 4, blue line) to the higher frequency mode (b, Figure 4 blue line) during t_2 followed by absorption from the higher frequency mode to the combination band (ab, Figure 4 blue line). Typically, peaks in this region are assigned to the off-diagonal anharamonicity, which arises from a transition from the first excited state manifold to a combination band in the second excited state manifold. However, since this assignment would conflict with the assignment of peak 3, we attribute this peak to rapid IVR between the two modes of the *cis*-B isomer. The transition frequencies determined from the 2DIR spectra are indicated in Figure 3 as solid lines and are given in Table 1.

Along with the transition frequencies we can also determine the relative magnitude of the transition dipole moments of the two modes of the *cis*-B isomer. From DFT calculations we determined that the angle between the two *cis*-B transition dipole moments is 87°. Since the measured angle only differs from 90° by 3°, we can approximate the magnitude of the transition dipole moments from the amplitudes of cross peak 4 and diagonal peak 2 at t_2 = 100 fs (in order to avoid contributions from overlapping pulses); details are given in the Supporting Information. We determined for the lower frequency mode the magnitude of the transition dipole moment to be 0.72 ± 0.02 D and for the higher frequency mode the magnitude to be 1.03 ± 0.02 D. Since the amplitude of the diagonal peak is proportional to $(1/15)|\mu_{0b'}|^2$-$[6|\mu_{0b'}|^2 + |\mu_{0b''}|^2]$, the relative amplitude of the diagonal peaks can be determined.[19] For the higher frequency mode the amplitude is 0.48, and the amplitude of the lower frequency peak is 0.14. This indicates that the contribution of the *cis*-B isomer to peak 1 is small and that peak 1 is mostly attributed to the *trans*-B isomer.

The results of the DFT calculations (Figure 5) support our experimental results. The optimized structures along with the relative change in enthalpy and Gibbs free energy are shown in Figure 5 for $Cp_2Fe_2(CO)_4$, and the Cartesian coordinates for the optimized geometries are given in the Supporting Information. The *trans*-B and *cis*-B isomers lie lowest in energy with the two nonbridging isomers lying higher in energy. The *trans*-NB isomer lies ΔG = 2.34 kcal/mol higher than the *trans*-B isomer. This is consistent with previous computational studies performed on the *trans*-B, *trans*-NB, and *cis*-B isomers.[20] This value for ΔG corresponds to an equilibrium constant of 0.02, indicating that the relative populations of the nonbridging isomers are negligible compared to the bridging isomers, and explains why we do not see any signature from the *trans*-NB isomer in our spectra. Previous

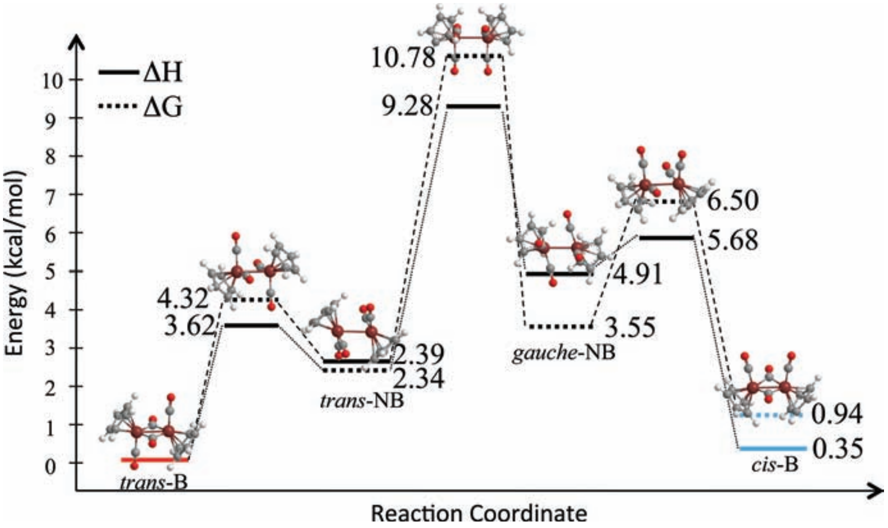

Figure 5. DFT-calculated ground state energies of $Cp_2Fe_2(CO)_4$ along with the corresponding transition states. Calculated ΔG (dashed lines) and ΔH (solid lines) are indicated.

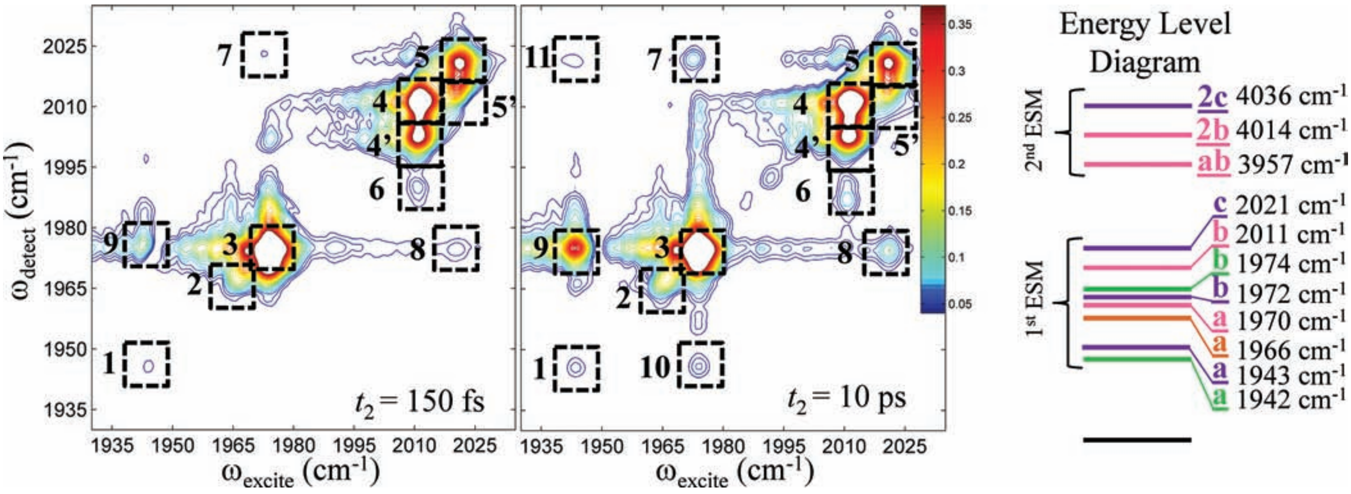

Figure 6. Absolute-value nonrephasing spectra of $Cp_2Ru_2(CO)_4$ in *n*-hexane at t_2 = 150 fs and 10 ps. Spectra are normalized to the maximum peak at the given t_2 value, and 30 contours are plotted for each spectrum.

studies did see evidence of the *trans*-NB isomer but indicated that the amount present was negligibly small (<0.1%), which is also consistent with our DFT calculations. The equilibrium constant for the *gauche*-NB isomer is 0.002, leading to an even smaller population, and is consistent with its absence in IR studies.

We also calculated the activation barriers associated with interconversion between the different stable isomers. For *trans*-B to *trans*-NB E_a = 3.62 kcal/mol, and for the *cis*-B to *gauche*-NB E_a = 5.33 kcal/mol. Previous NMR studies have observed bridging terminal carbonyl exchange with a *trans*-B to *trans*-NB activation energy of E_a = 6.5 kcal/mol.[8] Those studies also observed exchange between the two nonbridging forms, with an activation energy of 6.2 kcal/mol for *trans*-NB to *gauche*-NB.[8] This value is comparable to the DFT calculations, which predict an activation energy of 6.89 kcal/mol. Previous NMR studies have also observed the chemical exchange between the two bridging forms and determined the activation energy to be 16.7 kcal/mol.[6g] From our DFT calculations, the activation energy for the *trans*-B to *cis*-B isomer is 11.28 kcal/mol and for the reverse reaction *trans*-B to *cis*-B is 11.75 kcal/mol. We offer two possible reasons for the disagreement between the experimental and the calculated activation energies. One reason for disagreement could be due to the fact that the DFT calculations were performed in vacuum and do not take into account the influence of the solvent molecules. Another reason for the discrepancies could be due to the fact that the dynamic and static solvent effects were not taken into account in either of the previous NMR studies (see Supporting Information for more detail).

B. $Cp_2Ru_2(CO)_4$. The linear FTIR spectrum of $Cp_2Ru_2(CO)_4$ in the terminal carbonyl stretching region is shown in Figure 3b. Previous studies[6f,g] have assigned peak 1 at 1945 cm^{-1} to the *trans*-NB and *gauche*-NB isomers. Peak 2 at 1965 cm^{-1} was assigned to the *trans*-B. Three components were assigned to peak 3 at 1974 cm^{-1}: the *trans*-NB, *gauche*-NB, and *cis*-B isomers. Peak 4 at 2011 cm^{-1} was assigned the *cis*-B isomer, and peak 5 at 2021 cm^{-1} was assigned to the *gauche*-NB form. The modes

Table 3. Excitation and Detection Frequencies Obtained by Fitting the Peaks in Slices Taken from the 2D Spectra to Lorentzian Line Shapes

peak	ω_{excite}	ω_{detect}
1	1943.2 ± 0.2	
2	1965.9 ± 0.1	
3	1973.7 ± 0.1	
4	2011.2 ± 0.1	2011.2 ± 0.1
4′	2010.8 ± 0.1	2003.1 ± 0.1
5	2020.8 ± 0.1	2021.0 ± 0.0
5′	2021.1 ± 0.1	2015.5 ± 0.1
6	2010.5 ± 0.2	1986.8 ± 0.4
7	1972.4 ± 0.4	
8	2020.8 ± 0.9	
9	1941.9 ± 0.5	
10	1973.8 ± 0.1	1946.2 ± 0.1
11	1942.4 ± 1.3	

associated with these peaks are described in the Supporting Information.

The IR spectra of $Cp_2Ru_2(CO)_4$ are more complex than the iron analog due to the significant populations of the two nonbridging isomers. For the two complexes the metal atoms lie within group 8 of the periodic table, leading to similar bonding in the two complexes. However, the metals differ in row, with the ruthenium atom lying one row below the iron atom. This leads to differences in the metal–metal and metal–carbon bond lengths with the bond lengths of the ruthenium complex being slightly larger. This difference leads to a larger population of the nonbridging isomers for the ruthenium complex. Though the osmium analog is not the subject of the current study, it is known to exist only as the nonbridging forms because of the still further increase in the metal–metal and metal–carbon bond lengths.[6f]

The absolute value of the 2DIR nonrephasing spectra of $Cp_2Ru_2(CO)_4$ in hexane at t_2 = 150 fs and 10 ps are shown in Figure 6. To highlight the higher frequency peaks, the incoming pulses were tuned to the higher frequency peaks, leading to skewed 2DIR spectra when compared to the linear spectra. Because of the tuning of the incoming pulses, the amplitudes of the higher frequency peaks compared to the lower frequency peaks in the 2DIR spectra seem larger than what would be predicted from the linear FT-IR spectra. We choose to tune the incoming pulses to highlight the peaks in the upper left corner because this region is the least congested part of the spectrum due to the fact that there is reduced overlap with anharmonically shifted excited state absorptions. The conjugate cross peaks, which would appear in the lower right part of the spectrum, contain the same information but tend to have more contributions from the other peaks in the spectrum, including the anharmonically shifted diagonal peaks. Since the peaks contain the same information we choose the upper left of the spectrum to avoid complications of accounting for dynamics of overlapping peaks. One of the benefits associated with tuning the incoming beams is to highlight the weak cross peaks; however, unlike the case for $Cp_2Fe_2(CO)_4$, we are unable to determine the relative amplitudes of the dipole moments for the $Cp_2Ru_2(CO)_4$ complex due to tuning of the incoming pulses. The peaks along the diagonal, peaks 1–5, correspond to those seen in the linear FT-IR spectrum. Figure 6 also displays an energy level diagram depicting information regarding the transition frequencies that can be obtained from the 2DIR spectrum for both the first and the second excited state manifold. Peaks 4′ and 5′ are due to excited state absorptions (Figure 6) from b (pink) to 2b (pink) and from c (purple) to 2c (purple). Peaks 6, 7, 8, and 9 are present at t_2 = 150 fs, and as t_2 increases we see the appearance of peaks 10 and 11. Table 3 gives the transition frequencies obtained by fitting the peaks in slices taken from the 2D spectra to Lorentzian line shapes.

From the 2DIR spectra of $Cp_2Ru_2(CO)_4$ (Figure 6) it can be seen that the transition frequencies for the two bridging structures of $Cp_2Ru_2(CO)_4$ are shifted to higher frequencies compared to $Cp_2Fe_2(CO)_4$. The *trans*-B isomer is assigned to peak 2, and the *cis*-B isomer is assigned to peak 4 and has a small contribution to peak 3. The shift to higher frequencies can be simply explained by the increased bond length between the carbonyl carbon atoms and the metal atom. As the bond length increases, the carbonyl more closely resembles a free carbonyl group, shifting to higher frequency. We do not observe a clear cross peak between the two modes of the *cis*-B isomer; this may be due to the cross peak having contributions from the wings of diagonal peaks 3 and 4 which arise from scanning the t_1 time delay. However, we still see evidence that there are two modes from the *cis*-B isomer because of the presence of peak 6. Peak 6 arises from transitions to the combination band (Figure 6, ab (pink)). Though we cannot determine the transition frequency of the lower frequency mode of the *cis*-B isomer from the cross peaks, we can use the information obtained from the $Cp_2Fe_2(CO)_4$ complex in order to obtain the transition frequency. The frequency of the *trans*-B (1965.9 ± 0.1 cm^{-1}) and higher frequency (2011.2 ± 0.1 cm^{-1}) *cis*-B mode are shifted for the ruthenium complex; however, the spacing between the two modes only differs by ~1 cm^{-1} when compared to the frequency spacing in the iron complex, indicating that the lower frequency *cis*-B mode should also maintain the same frequency spacing. Using this comparison we determined a frequency of 1970 cm^{-1} for the lower frequency *cis*-B mode.

$Cp_2Ru_2(CO)_4$ also exists as two nonbridging forms at room temperature. Peaks 1 and 3 have some contribution from both the *trans*-NB and the *gauche*-NB form, and peak 5 is assigned the *gauche*-NB form alone. As was the case with the cartoon spectrum and for $Cp_2Fe_2(CO)_4$, we obtain the transition frequencies of the overlapping peaks from the cross peaks in the 2DIR spectra. In order to obtain the transition frequencies from the spectrum we fit to Lorenzians the peaks in slices taken along ω_{excite} for specific values of ω_{detect}. In the case for the iron complex, the anharmonic peaks (resulting from transitions between the first and the second excited state manifold) were well separated from the peaks resulting from transitions between the ground and the first excited state manifold. This is not the case for the ruthenium complex, and for this reason we choose to use the frequencies obtained from fitting the slices taken along the ω_{excite} axis for given values of ω_{detect}. In order to separate these transitions, an absorptive spectrum could be obtained; however, since we are able to extract the information from the absolute value nonrephasing spectra and it is beneficial to extract the IVR rate constants from the absolute value nonrephasing spectra, we did not obtain absorptive spectra.

Cross peaks 9 and 10 are inherent cross peaks arising from the two transitions of the *trans*-NB species. Peak 10 is not observed at t_2 = 150 fs, which we attribute to the tuning of the incoming pulses. With increased t_2, peak 10 becomes more prominent

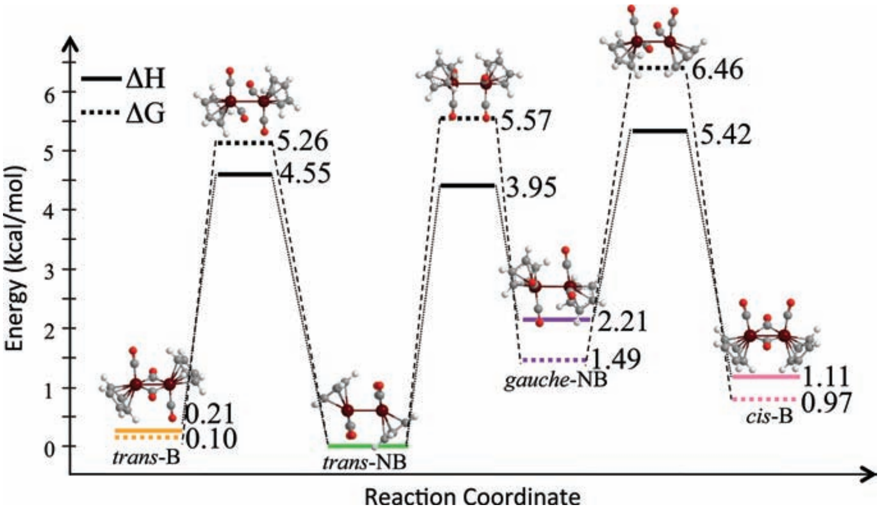

Figure 7. DFT-calculated ground state energies of $Cp_2Ru_2(CO)_4$ along with the corresponding transition states. Calculated ΔG (dashed lines) and ΔH (solid lines) are indicated.

because of IVR. From the position of cross peaks 9 and 10 the transition frequencies for the two modes of the *trans*-NB isomer are found to be 1941.9 ± 0.5 and 1973.8 ± 0.1 cm^{-1}. Cross peaks 7, 8, and 11 are inherent cross peaks arising from the three modes of the *gauche*-NB isomer. From the position of these peaks we can obtain the transition frequencies for the modes: 1942.4 ± 1.3, 1972.4 ± 0.4, and 2020.8 ± 0.9 cm^{-1}. We also compared our experimentally determined frequencies to the DFT-calculated frequencies. The frequencies are given in Table 1 and are represented graphically in Figure 3 with the experimental frequencies indicated as solid lines and the scaled DFT frequencies as dashed lines. The calculated frequencies differ from the experimentally determined frequencies by 7 cm^{-1} at most. In general, the relative ordering of the DFT-calculated frequencies is correct, except for the ordering of the frequencies making up peak 3.

Information on the second excited state manifold was also obtained for the *gauche*-NB isomer from peak 5′ and for the *cis*-B isomer from peaks 4′ and 6. An anharmonicity of ~6 cm^{-1} was obtained for the higher frequency mode of the *gauche*-NB isomer (c, Figure 6, purple. For the higher frequency mode of the *cis*-B isomer (b, Figure 6, pink) an anharmonicity of 8 cm^{-1} was obtained. From the anharmonicities the frequencies of the second excited state manifold were found to be 4036 (2c, purple, Figure 6) and 4014 cm^{-1} (2b, pink, Figure 6). Peak 6 is due to a transition from the first excited state manifold of the *cis*-B isomer to the corresponding combination band ab (pink, Figure 6). The anharmonicities of peaks 1, 2, and 3 are not attainable from the absolute value nonrephasing spectra. This is due to the smaller vibrational anharamonicity for these transitions, which results in more spectral overlap. A smaller vibrational anharmonicity leads to a smaller shift of the anharmonic peak along ω_{detect}, leading to inseparable diagonal and anharmonic peaks. It is for this same reason we are unable to clearly resolve the off-diagonal anharmonicities which result from transitions to the combination bands of the coupled modes.

We also performed DFT calculations on the isomers of $Cp_2Ru_2(CO)_4$ (Figure 7). Here, the *trans*-NB species lies lowest in energy with the *trans*-B species lying only slightly higher at ΔG = 0.10 kcal/mol. Previous experimental studies found that the *trans*-B species lies the lowest in energy.[6g] However, this energy difference is very small, and since the calculations are performed in vacuum, the solvent interactions may be capable of inverting the ordering of these energies. The *gauche*-B isomer lies the highest in energy at ΔG = 1.49 kcal/mol, which corresponds to an equilibrium constant of 0.08. Compared to the iron complex, the nonbridging species for the ruthenium complex lie lower in energy. One reason for this difference is that fact that the metal−metal bond length in the ruthenium complex is longer than that of the iron complex and the increased bond length leads to reduced steric hindrance resulting in a decrease in energy.

The activation barrier for isomerization between the different isomers was also calculated. For bridging terminal carbonyl exchange the activation energy for *trans*-B to *trans*-NB is E_a = 4.34 kcal/mol, and for *cis*-B to *gauche*-NB the activation energy is E_a = 4.31 kcal/mol. Previous NMR studies have determined the activation energy for bridging terminal carbonyl exchange to be 7.6 kcal/mol for *trans*-B to *trans*-NB and ~8.1 kcal/mol for *cis*-B to *gauche*-NB. Again, we do not see quantitative agreement, but we do see that the difference between the two calculated energies is smaller than the difference in energies for the iron complex, as is the difference in energy between the two experimentally determined energies when compared to the iron complex. DFT and experiment indicate that the barrier for rotation about the Ru−Ru bond is lower than it is about the Fe−Fe bond, which is consistent with the greater Ru−Ru bond length. The increased bond length results in reduced steric hindrance and reduced barrier to rotation about the metal−metal bond. The DFT-calculated barrier is 3.95 kcal/mol for the *trans*-NB to *gauche*-NB interconversion. Previous NMR studies have suggested the barrier to be below 5 kcal/mol; however, these studies were not able to determine the barrier directly because the process was occurring on a time scale that was faster than could be probed with NMR.[6g,8] Barrier heights of this magnitude generally correspond to picosecond time scales for interconversion, which in principle may be observable using 2DIR spectroscopy. In this study, however, we do not observe exchange between the two nonbridging forms.

II. Intramolecular Vibrational Energy Redistribution. The intramolecular vibrational energy redistribution between the two

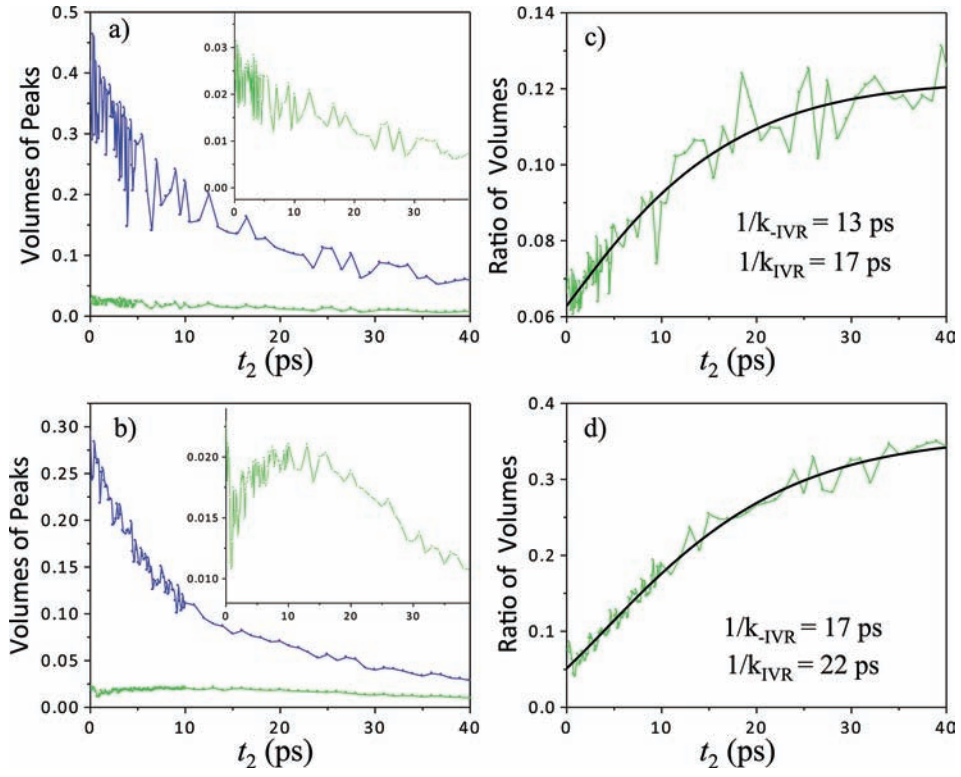

Figure 8. (a) Plot of the volumes of peaks 2 (blue) and 4 (green) for $Cp_2Fe_2(CO)_4$ in *n*-hexane. (b) Plot of the volumes of peaks 5 (blue) and 7 (green) for $Cp_2Ru_2(CO)_4$ in *n*-hexane. (c) Plot of the ratio of cross peak 4 to diagonal peak 2 for $Cp_2Fe_2(CO)_4$ (green) along with the resulting fit to eq 2 (black). (d) Plot of the ratio of cross peak 7 to diagonal peak 5 for $Cp_2Ru_2(CO)_4$ (green) along with the resulting fit to eq 2 (black).

higher frequency modes of the *gauche*-NB isomer for $Cp_2Ru_2(CO)_4$ and between the modes of the *cis*-B isomer for $Cp_2Fe_2(CO)_4$ was also studied. We chose to study the *gauche*-NB modes for the $Cp_2Ru_2(CO)_4$ complex because the cross peak, peak 7, and corresponding diagonal peak, peak 5, are in the least congested region of the spectrum. There are three coupled modes for the *gauche*-NB isomer; however, we only looked at the IVR between two higher frequency coupled modes (see Supporting Information for more details).

From Figures 8a and 8b we see that for both metal complexes the diagonal peaks (blue) decay due to molecular reorientation, vibrational population relaxation, and IVR. The cross peaks (green) behave differently for the two metal complexes. For $Cp_2Fe_2(CO)_4$ the cross-peak decays. When compared to the corresponding diagonal peak the extent of decay is diminished, which is attributed to the IVR process that contributes to growth of the cross peak. For $Cp_2Ru_2(CO)_4$, the cross peak first grows in and then decays. At very early waiting times, the volume of the cross peak seems to decrease suddenly due to artifacts arising from time overlap of the incoming pulses. Following pulse overlap, the decay is due to molecular reorientation and population relaxation. There are two possible origins for the signal growth. As discussed previously, the barrier for interconversion between these two species is consistent with picosecond exchange arising from isomerization. The growth could be due to either exchange between the two nonbridging species or IVR between the two modes of the *gauche*-NB isomer. By comparing the excitation frequency of the cross peak to the transition frequencies for the *trans*-NB isomer along with examining how the cross-peak growth changes with solvent, we assign the growth to IVR. A detailed account of this assignment is given in the Supporting Information.

Previous NMR experiments[8] and our DFT calculations indicate that chemical exchange between the *gauche*-NB and *trans*-NB isomer occurs on the picosecond time scale (a barrier of less than 5 kcal/mol). To further investigate why chemical exchange is not observed, we simulated the waiting time-dependent amplitude of two diagonal peaks and the corresponding exchange cross peak. Using a simple kinetic model (details are given in the Supporting Information), where two states, A and B, interconvert with forward and reverse rate constants, k_{for} and k_{rev}, and vibrationally decay with a rate constant k_{Vib}, we determined an expression for the maximum amplitude that would be due to the exchange signal for the cross peak at $\omega_{excite} = \omega_A$, $\omega_{detect} = \omega_B$ (eq 1), where $k_{Sum} = k_{for} + k_{rev} + k_{Vib}$ and B_0 is the initial effective population. We choose to use the effective population here to avoid accounting for the concentration, oscillator strength, and tuning of the incoming pulses separately.

$$S_{max} = \frac{B_0 k_{for} \left(\dfrac{k_{sum}}{k_{Vib}}\right)^{-\left(\dfrac{k_{sum}}{k_{for} + k_{rev}}\right)}}{k_{Vib}} \qquad (1)$$

The initial effective population, B_0, was set to be equal to the initial amplitude of peak 5, and k_{rev} was set to be equal to 0.050 ps^{-1}. The forward rate constant, k_{for}, is related to k_{rev} through the equilibrium constant, K_{eq}, $k_{for} = k_{rev}/K_{eq}$, where $K_{eq} = 0.08$ was obtained from our DFT calculations. The rate constant associated with vibrational population relaxation was set to 0.050 ps^{-1}. This value was determined by fitting the

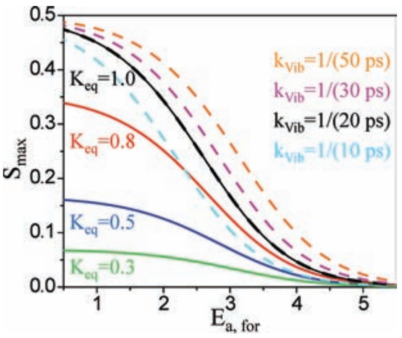

Figure 9. Maximum amplitude of exchange plotted versus barrier height for K_{eq} = 1 in black. (Solid lines) Maximum amplitude of exchange for k_{Vib} = 0.05 ps^{-1} and K_{eq} = 0.8 (red), 0.5 (blue), and 0.3 (green). (Dashed line) Maximum amplitude of exchange for K_{eq} = 1 and k_{Vib} = 0.02 (orange), 0.03 (magenta), and 0.10 ps^{-1} (cyan).

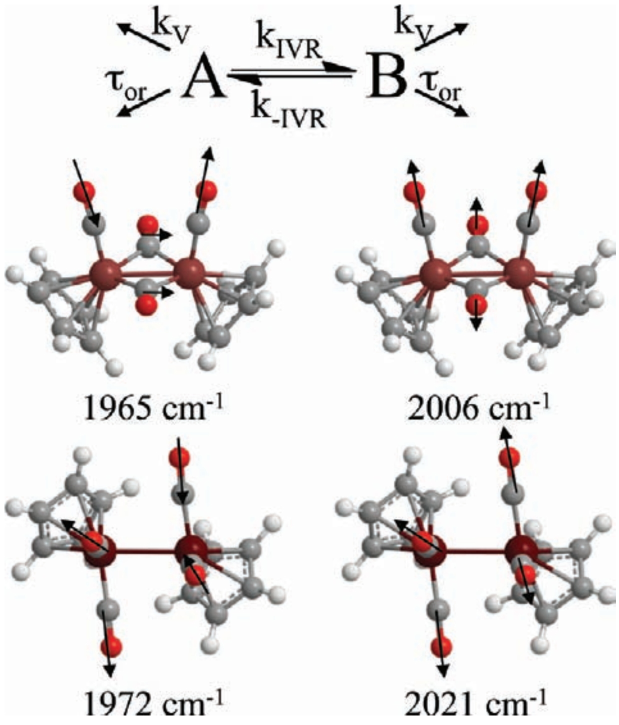

Figure 10. (Top) Kinetic model used to describe the IVR process. (Bottom) Vibrational modes involved in the IVR process are shown for $Cp_2Fe_2(CO)_4$ and $Cp_2Ru_2(CO)_4$. Arrows indicate displacements of the carbonyl units.

waiting time-dependent volume of the diagonal peak 3 to a biexponential, taking the long-time decay to be due vibrational population relaxation. Using these values, we are able to approximate the maximum amplitude of the exchange signal contributing to cross peak 7 to be only 1.9% of the maximum amplitude of diagonal peak 5. This model shows that one impediment to observing exchange is the small equilibrium population of the *gauche*-NB isomer.

In order to explore how the different parameters affect the amplitude of the exchange signal, we plotted the maximum amplitude of exchange versus the activation energy associated with the forward reaction, where the forward rate constant is related to the activation energy by transition state theory ($k_{for} = ((kT)/h)\exp(-E_{a,for}/RT)$, where k is Boltzmann's constant, h is Planck's constant, T is the temperature, and R is the ideal gas constant) in Figure 9. Here, we neglected oscillator strength and tuning of the incoming pulses by taking B_0 to be equivalent to the equilibrium constant. The maximum amplitude of exchange as a function of barrier height ranging from 0.5 to 5.5 kcal/mol for k_{Vib} = 0.05 ps^{-1} and K_{eq} = 1 is plotted in black. As the barrier height increases, we see the amplitude of the signal decreases and approaches zero at ∼5 kcal/mol. Varying K_{eq} (keeping k_{Vib} = 0.05 ps^{-1}) we find the maximum amplitude of the exchange signal decreases as K_{eq} decreases (solid lines Figure 9); as the population of species B decreases with respect to species A, the maximum amplitude of the exchange signal also decreases. Varying k_{Vib} (keeping K_{eq} = 1), we find that the window for which exchange can be observed increases as k_{Vib} decreases (dashed lines in Figure 9). It is important to note that eq 1 predicts the maximum possible exchange signal and that this model does not account for the redistribution of vibrational energy upon isomerization (Supporting Information).

It is also important to note that the conjugate cross peak, peak 8, would have an enhanced exchange contribution according to the simple model; the equation corresponding to the maximum amplitude of exchange signal from this cross peak is given in the Supporting Information. However, we choose not to focus on cross peak 8 because it is in the more congested region of the spectrum and is already being influenced by the wings of diagonal peak 3.

Though we do not observe exchange, we do observe IVR. To extract the IVR rate constants we modeled IVR as an equilibrium process. The kinetic model we used is given in Figure 10, where k_V is the rate of vibrational population relaxation, τ_{or} is the molecular reorientation time, k_{IVR} and k_{-IVR} are the forward and reverse rate constants for IVR, *A* indicates the lower frequency mode involved in the IVR process, while *B* indicates the higher frequency mode. The solutions to this equation have been given previously and are briefly described in the Supporting Information. In order to reduce the number of fitting parameters, we took the ratio of the amplitude of the upper left cross peak to the higher frequency diagonal peak, eliminating the population relaxation term. The molecular reorientation times were determined from molecular dynamics (MD) simulations for the *gauche*-NB isomer for $Cp_2Ru_2(CO)_4$ (see Supporting Information). We used this molecular reorientation time for both the $Cp_2Ru_2(CO)_4$ and the $Cp_2Fe_2(CO)_4$ complexes since we do not expect the molecular reorientation time to change significantly between the two species. Also, we found that varying the molecular reorientation time by ±10 ps results in the variation of the rate constants by 2% at the most. To obtain the IVR rate constants we fit our data to the following equation allowing for the following 4 parameters to vary: *A*, k_{-IVR}, N_A, N_B.

$$\begin{aligned} S_{CP/DP}(t_2) = {} & A(3 + 5e^{6D_{or}t_2})(N_A g - N_B h \\ & + h(N_A + N_B)e^{(k_{IVR} + k_{-IVR})t_2})/2N_B(4 \\ & + 5e^{6D_{or}t_2})(h + g e^{(k_{IVR} + k_{-IVR})t_2}) \end{aligned} \qquad (2)$$

In the above equation, *A* is the amplitude of the inherent cross peak, $6D_{or} = 1/\tau_{or}$, $k_{IVR} = k_{-IVR}\exp(-\Delta cm^{-1}/207\ cm^{-1})$, where Δcm^{-1} is the splitting between the two modes involved, N_A is the effective initial population of A, and N_B is the effective initial population of mode B, $g = k_{\mathrm{IVR}}/(k_{\mathrm{IVR}} + k_{-\mathrm{IVR}})$, and $h = k_{-\mathrm{IVR}}/(k_{\mathrm{IVR}} + k_{-\mathrm{IVR}})$.

The ratios of the volumes of the peaks along with the fits obtained from fitting to the above equation are shown in Figure 8c and 8d. For $Cp_2Fe_2(CO)_4$, the IVR rate constants for energy exchange between the two modes of the *cis*-B isomer were determined to be $k_{-\mathrm{IVR}} = 0.072 \pm 0.012$ ps^{-1} (14 ± 3 ps) and $k_{\mathrm{IVR}} = 0.059 \pm 0.013$ ps^{-1} (17 ± 5 ps). The two modes involved are shown in Figure 10. The higher frequency mode is the symmetric stretch of the terminal carbonyls, and the lower frequency mode is the antisymmetric stretch of the terminal carbonyls. For $Cp_2Ru_2(CO)_4$, the IVR rates between the two modes of the *gauche*-NB were determined to be $k_{-\mathrm{IVR}}= 0.057 \pm 0.007$ ps^{-1} (17 ± 2 ps) and $k_{\mathrm{IVR}}= 0.045 \pm 0.007$ ps^{-1} (22 ± 4 ps). The two modes involved are shown in Figure 10. The higher frequency mode is the symmetric stretch, and the lower frequency mode is the antisymmetric stretch.

For both metal complexes, we find that the IVR rate constant is slower for the uphill transfer compared to the downhill transfer, which is due to the weighting by the Boltzmann factor. To within the error bars, these rate constants are the same, which is due to the relatively small splitting between the two modes. As the splitting between the modes increases, we would expect to see a larger difference between the uphill and the downhill rate constants associated with energy transfer. We also find that for the ruthenium complex the rate of IVR is slightly slower compared to the iron complex. One of the main differences between the two metal complexes is the difference in frequency between the two modes involved. For $Cp_2Fe_2(CO)_4$ the difference in frequency is 41 cm^{-1}, and for $Cp_2Ru_2(CO)_4$ it is 49 cm^{-1}. Assuming that the rate of IVR is directly proportional to the population of liquid phonons at an energy corresponding to the difference in energy between the two modes involved in IVR,[2a,21] we find that the rate of IVR for a splitting of 41 cm^{-1} should decrease by 18% as the splitting is increased to 49 cm^{-1}. The measured IVR rate constant for $Cp_2Ru_2(CO)_4$ is 21 ± 10% slower than that of $Cp_2Fe_2(CO)_4$. The agreement with the simple description of IVR as a barrierless process free of solvent−solute interactions indicates that the linear alkane solvents do not modify the solvation shell environment or the associated energetics. This lack of solvent specificity contrasts our recent observation of solvent-hindered vibrational energy redistribution in metal carbonyl complexes in hydrogen-bonding alcohols.[4] The present work lays the foundation for future studies in more strongly interacting solvents capable of forming hydrogen bonds with the complex.

CONCLUSION

Congested linear IR spectra obscure the assignment of peaks requiring several solvent- and temperature-dependent spectra to determine the contributions from different species to individual spectral features. Even with such data, the precise transition frequencies of the contributing species may be difficult to extract unambiguously. In this manuscript we utilized 2DIR spectroscopy to aid in the interpretation of the linear FT-IR spectrum for $Cp_2Fe_2(CO)_4$ and $Cp_2Ru_2(CO)_4$. The iron and ruthenium complexes belong to the same group of the periodic table and are structurally related complexes whose energetics and IR spectra differ due primarily to the metal−metal bond distance, which increases from the iron to the ruthenium complex. Using 2DIR spectroscopy combined with DFT calculations we explored the energetic and structural consequences of this periodic trend. From the 2DIR spectrum we are able to obtain the transition frequencies for the individual isomers from inherent cross peaks in the spectra, and in combination with DFT results, this leads to a detailed understanding of the spectroscopic and energetic differences between these two metal complexes.

Not only do the cross peaks aid in assignment but also by monitoring the picosecond-scale changes in the volumes of the cross peaks as a function of waiting time we are able to obtain the rate of vibrational energy transfer (IVR) for both the uphill and the downhill transfer of energy. We find the rate of IVR for the iron complex is faster compared to the ruthenium complex, consistent with an explanation based solely on the energy gap between the two modes.

Though we did see energy transfer in both complexes, we did not see any population transfer between distinct chemical species due to chemical exchange. However, the DFT calculations and previous NMR experiments suggest that it should be possible to observe chemical exchange between the *gauche*-NB and the *trans*-NB forms of $Cp_2Ru_2(CO)_4$ on the time scale probed by 2DIR spectroscopy. We propose that our inability to observe exchange is due to the very small population of the *gauche*-NB form. One way to address this issue in future work would be to perform the experiment in solvents that stabilize the polar isomers, namely, the *gauche*-NB and *cis*-B isomers, increasing the population of the *gauche*-NB isomer relative to the *trans*-NB. If the relative free energies of the two isomers were equal, we predict that the amplitude of the exchange signal would increase by an order of magnitude (i.e., to 10% of the maximum of diagonal peak 5). Performing the experiments using different solvents may facilitate observation of chemical exchange while perhaps introducing a structured solvation shell environment to spatially modulate the reaction barrier and vibrational energy transfer. This work emphasizes the power that 2DIR spectroscopy has to resolve structure and dynamics in condensed phase systems, which is crucial information needed to understand current inorganic-based catalysis as well as design future catalysts. For metal carbonyl complexes, which often have vibrational lifetimes exceeding 50−100 ps, 2DIR offers a promising avenue to investigate subtle structural, energetic, and dynamical differences on energy scales below 5 kcal/mol in solution and at room temperature.

ASSOCIATED CONTENT

Ⓢ Supporting Information. DFT-calculated structures and coordinates, background on the amplitudes of diagonal and cross peaks, difference between rephasing and nonrephasing spectra, waiting time-dependent step sizes, details of the basis sets, static versus dynamic solvent effect, details on assigning cross-peak growth, information on the maximum exchange signal, details on the two-state kinetic model, and details on the kinetic model used to treat the IVR process. This material is available free of charge via the Internet at http://pubs.acs.org.

AUTHOR INFORMATION

Corresponding Author

*E-mail: kubarych@umich.edu.

ACKNOWLEDGMENT

This work was supported by the National Science Foundation (CHE-0748501) and the Camille & Henry Dreyfus Foundation.

J.M.A. acknowledges support from a Rackham One-Term Fellowship.

■ REFERENCES

(1) (a) Drage, J. S.; Tilset, M.; Vollhardt, P. C.; Weidman, T. W. *Organometallics* **1984**, *3*, 812. (b) Boese, R.; Cammack, J. K.; Matzger, A. J.; Pflug, K.; Tolman, W. B.; Vollhardt, K. P. C.; Weidman, T. W. *J. Am. Chem. Soc.* **1997**, *119*, 6757. (c) Kanai, Y.; Srinivasan, V.; Meier, S. K.; Vollhardt, K. P. C.; Grossman, J. C. *Angew. Chem., Int. Ed.* **2010**, *49*, 8926. (d) Kong, Q.; Lee, J. H.; Kim, K. H.; Kim, J.; Wulff, M.; Ihee, H.; Koch, M. H. J. *J. Am. Chem. Soc.* **2010**, *132*, 2600. (e) Stewart, A. I.; Wright, J. A.; Greetham, G. M.; Kaziannis, S.; Santabarbara, S.; Towrie, M.; Parker, A. W.; Pickett, C. J.; Hunt, N. T. *Inorg. Chem.* **2010**, *49*, 9563. (f) Baiz, C. R.; McCanne, R.; Nee, M. J.; Kubarych, K. J. *J. Phys. Chem. A* **2009**, *113*, 8907.

(2) (a) Cahoon, J. F.; Sawyer, K. R.; Schlegel, J. P.; Harris, C. B. *Science* **2008**, *319*, 1820. (b) Anna, J. M.; Ross, M. R.; Kubarych, K. J. *J. Phys. Chem. A* **2009**, *113*, 6544. (c) Baiz, C. R.; McCanne, R.; Kubarych, K. J. *J. Am. Chem. Soc.* **2009**, *131*, 13590.(d) Anna, J. M.; Kubarych, K. J. *J. Chem. Phys.* **2010**, *133*, 174506. (e) Kania, R.; Stewart, A. I.; Clark, I. P.; Greetham, G. M.; Parker, A. W.; Towrie, M.; Hunt, N. T. *Phys. Chem. Chem. Phys.* **2010**, *12*, 1051.

(3) Bredenbeck, J.; Helbing, J.; Hamm, P. *J. Am. Chem. Soc.* **2004**, *126*, 990.

(4) King, J. T.; Anna, J. M.; Kubarych, K. J. *Phys. Chem. Chem. Phys.* **2011**, *13*, 5579.

(5) Jaworska, M.; Macyk, W.; Stasicka, Z. *Struct. Bonding* **2004**, *106*, 153.

(6) (a) Piper, T. S.; Cotton, F. A.; Wilkinson, G. *J. Inorg. Nucl. Chem.* **1955**, *1*, 165. (b) Cotton, F. A.; Stammreich, H.; Wilkinson, G. *J. Inorg. Nucl. Chem.* **1959**, *9*, 3. (c) Noack, K. *J. Inorg. Nucl. Chem.* **1963**, *25*, 1383. (d) Cotton, F. A.; Yagupsky, G. *Inorg. Chem.* **1967**, *6*, 15. (e) Manning, A. R. *J. Chem. Soc. A* **1968**, 1319. (f) McArdle, P.; Manning, A. R. *J. Chem. Soc. A* **1970**, 2128. (g) Bullitt, J. G.; Cotton, F. A.; Marks, T. J. *Inorg. Chem.* **1972**, *11*, 671.

(7) (a) Mills, O. S. *Acta Crystallogr.* **1958**, *11*, 620. (b) Mills, O. S.; Nice, J. P. *J. Organomet. Chem.* **1967**, *9*, 339. (c) Bryan, R. F.; Greene, P. T. *J Chem Soc A* **1970**, 3064. (d) Bryan, R. F.; Greene, P. T.; Newlands, M. J.; Field, D. S. *J. Chem. Soc. A* **1970**, 3068. (e) Mague, J. T. *Acta Crystallogr., C* **1995**, *51*, 831.

(8) Gansow, O. A.; Burke, A. R.; Vernon, W. D. *J. Am. Chem. Soc.* **1976**, *98*, 5817.

(9) Bitterwolf, T. E. *Coord. Chem. Rev.* **2000**, *206*, 419.

(10) (a) Woutersen, S.; Mu, Y.; Stock, G.; Hamm, P. *Chem. Phys.* **2001**, *266*, 137. (b) Khalil, M.; Demirdoven, N.; Tokmakoff, A. *J. Phys. Chem. A* **2003**, *107*, 5258. (c) Hamm, P.; Helbing, J.; Bredenbeck, J. *Annu. Rev. Phys. Chem.* **2008**, *59*, 291. (d) Fayer, M. D. *Annu. Rev. Phys. Chem.* **2009**, *60*, 21. (e) Kim, Y. S.; Hochstrasser, R. M. *J. Phys. Chem. B* **2009**, *113*, 8231. (f) Roberts, S. T.; Ramasesha, K.; Tokmakoff, A. *Acc. Chem. Res.* **2009**, *42*, 1239. (g) Strasfeld, D. B.; Ling, Y. L.; Gupta, R.; Raleigh, D. P.; Zanni, M. T. *J. Phys. Chem. B* **2009**, *113*, 15679. (h) King, J. T.; Baiz, C. R.; Kubarych, K. J. *J. Phys. Chem. A* **2010**, *114*, 10590.

(11) (a) Jonas, D. M. *Annu. Rev. Phys. Chem.* **2003**, *54*, 425. (b) Cho, M. H. *Chem Rev* **2008**, *108*, 1331.

(12) Kim, Y. S.; Hochstrasser, R. M. *Proc. Natl. Acad. Sci. U.S.A.* **2005**, *102*, 11185.

(13) (a) Zheng, J.; Kwak, K.; Asbury, J.; Chen, X.; Piletic, I.; Fayer, M. *Science* **2005**, *309*, 1338. (b) Zheng, J.; Kwak, K.; Xie, J.; Fayer, M. *Science* **2006**, *313*, 1951.

(14) Asbury, J. B.; Steinel, T.; Fayer, M. D. *Chem. Phys. Lett.* **2003**, *381*, 139.

(15) (a) Nee, M. J.; McCanne, R.; Kubarych, K. J.; Joffre, M. *Opt. Lett.* **2007**, *32*, 713. (b) Anna, J. M.; Nee, M. J.; Baiz, C. R.; McCanne, R.; Kubarych, K. J. *J. Opt. Soc. Am. B* **2010**, *27*, 382.

(16) Frisch, M. J.; Trucks, G. W.; Schlegel, H. B.; Scuseria, G. E.; Robb, M. A.; Cheeseman, J. R.; Montgomery, J., J. A.; Vreven, T.; Kudin, K. N.; Burant, J. C.; Millam, J. M.; Iyengar, S. S.; Tomasi, J.; Barone, V.; Mennucci, B.; Cossi, M.; Scalmani, G.; Rega, N.; Petersson, G. A.; Nakatsuji, H.; Hada, M.; Ehara, M.; Toyota, K.; Fukuda, R.; Hasegawa, J.; Ishida, M.; Nakajima, T.; Honda, Y.; Kitao, O.; Nakai, H.; Klene, M.; Li, X.; Knox, J. E.; Hratchian, H. P.; Cross, J. B.; Bakken, V.; Adamo, C.; Jaramillo, J.; Gomperts, R.; Stratmann, R. E.; Yazyev, O.; Austin, A. J.; Cammi, R.; Pomelli, C.; Ochterski, J. W.; Ayala, P. Y.; Morokuma, K.; Voth, G. A.; Salvador, P.; Dannenberg, J. J.; Zakrzewski, V. G.; Dapprich, S.; Daniels, A. D.; Strain, M. C.; Farkas, O.; Malick, D. K.; Rabuck, A. D.; Raghavachari, K.; Foresman, J. B.; Ortiz, J. V.; Cui, Q.; Baboul, A. G.; Clifford, S.; Cioslowski, J.; Stefanov, B. B.; Liu, G.; Liashenko, A.; Piskorz, P.; Komaromi, I.; Martin, R. L.; Fox, D. J.; Keith, T.; Al-Laham, M. A.; Peng, C. Y.; Nanayakkara, A.; Challacombe, M.; Gill, P. M. W.; Johnson, B.; Chen, W.; Wong, M. W.; Gonzalez, C.; Pople, J. A. *Gaussian03*; Gaussian, Inc.: Wallingford, CT, 2004.

(17) Peng, C. Y.; Schlegel, H. B. *Isr. J. Chem.* **1993**, *33*, 449.

(18) (a) Fischer, R. D.; Vogler, A.; Noack, K. *J. Organomet. Chem.* **1967**, *7*, 135. (b) Noack, K. *J. Organomet. Chem.* **1967**, *7*, 151.

(19) Golonzka, O.; Tokmakoff, A. *J. Chem. Phys.* **2001**, *115*, 297.

(20) Wang, H. Y.; Xie, Y. M.; King, R. B.; Schaefer, H. F. *Inorg. Chem.* **2006**, *45*, 3384.

(21) Tokmakoff, A.; Sauter, B.; Fayer, M. D. *J. Chem. Phys.* **1994**, *100*, 9035.